Design, optimization and numerical modelling of a novel floating pendulum wave energy converter with tide adaptation

Jing Yang[1], Dahai Zhang[1,2,*], Hui Liang[1], Ying Chen[1,2], Ming Tan[1], Wei Li[2], Xiandong Ma[3]

1. Ocean College, Zhejiang University, China
2. The State Key Laboratory of Fluid Power and Mechatronic Systems, Zhejiang University, China
3. Engineering Department, Lancaster University, Lancaster, UK, LA1 4YR

Abstract:

A novel floating pendulum wave energy converter (WEC) with the ability of tide adaptation is designed and presented in this paper. Aiming to a high efficiency, the buoy's hydrodynamic shape is optimized by enumeration and comparison. Furthermore, in order to keep the buoy's well-designed leading edge always facing the incoming wave straightly, a novel transmission mechanism is then adopted, which is called tide adaptation mechanism in this paper. Time domain numerical models of floating pendulum WEC with or without tide adaptation mechanism are built to compare their performance on various water levels. When comparing these two WECs in terms of their average output based on linear passive control strategy, the output power of WEC with tide adaptation mechanism is much steadier with the change of water level and

* Corresponding author at: Institute of Ocean Engineering and Technology, Ocean College, Zhoushan Campus, Zhejiang University, Zhoushan 316000, China.
Tel.: +86 13758255738; Fax: +86 0580 2092891
E-mail address: zhangdahai@zju.edu.cn (D. Zhang)

always larger than that without tide adaptation mechanism.

Keywords:

Wave energy, Simulation, Model analysis, Tide adaptation

Nomenclature

A	real-time wave height	M_{PTO}	reacting moment of power-take-off
a_{33}	added mass	M_{chain}	moment applied by the chain
b_{33}	radiation damping coefficient of heave	$\boldsymbol{n}$	unit normal vector of element dS
CFD	computational fluid dynamics	OWC	oscillating water column
C_D	drag coefficient	O_A	pivot point on the base
Cw	capture width	O_B	pivot point on the buoy
c_{pto}	coefficient of power-take-off	P_{WEC}	absorbed power by WEC
g	gravity acceleration	P_{wave}	wave energy per unit width
H	wave height	p_b	hydrostatic pressure
h	depth of water tank	p_e	excitation pressure
h_0	displacement depth of O_A	$\boldsymbol{q}$	position vector of element dS against O_A
J_A	rotational inertia about pivot point O_A	$\boldsymbol{s}$	position vector of element dS against O_B
k	wave number	T	wave period
l	distance between O_A and O_B	u	velocity of the water particle
l_{GA}	distance between the center	u_b	velocity of the buoy

	of gravity of the immersed part of the buoy and O_A		
l_{GB}	distance between the center of gravity of the immersed part of the buoy and O_B	WEC	Wave Energy Converter
m	mass of buoy	λ	wavelength
M_e	excitation moment	ρ	water density
M_r	radiated moment	ρ_{buoy}	density of buoy
M_b	hydrostatic moment	ω	wave frequency
M_d	drag moment	θ	rotational angle

1. Introduction

Ocean wave energy is regarded as one of the most promising sustainable sources. Its practical worldwide potential is projected to be 93−100 trillion kilowatt hours per year (Arman and Yuksel, 2013). The World Energy Council estimates that about 10% of worldwide electricity demand could be met by harvesting ocean energy (World Energy Council, 1993). With global attention now being drawn to climate change and green house effect, wave energy exploitation is becoming an increasing concern. A considerable number of large-scale exploitation of wave energy have been deployed until now. Devices like Pelamis, Archimedes Wave Swing (AWS) have already started to deliver offshore wave power to a national electricity grid (Henderson, 2006; Valério et al., 2008). Although problems like high cost and low efficiency still exist, wave energy is believed to be more competitive with the technology development and market promotion.

According to the deployment location, WECs can be classified into three types: shoreline devices, near-shore devices and offshore devices (Drew et al., 2009). Shoreline devices, by contrast, have the advantage of being close to the utility network,

and easy to maintain. However, waves will be attenuated as they run and break in shallow water. Tide range also has effect on efficiency of shoreline devices. A typical example of shoreline device is the Limpet oscillating water column (OWC) device. It is installed on the island of Islay, Scotland, and produces power for the national grid (Boake et al., 2002). The device consists of a chamber with an opening to the sea below the waterline. With the variation of the water level, air passes in and out the chamber that drives a turbine to generate electricity. Theoretically, the mass of water inside the chamber determines the water column resonance, which can be coupled to the predominant period of the incoming waves. Thus, water level changes caused by tides may influence its efficiency dramatically.

Another typical shoreline device is SDE wave power device, a shoreline device of the floating type, developed by S.D.E. Ltd in Israel. The incoming wave drives the floating buoy rotate around the axis that is fixed on the shore. The device takes advantages of both kinetic and potential energy of wave, the upper bound of its efficiency is theoretically higher (Clément et al., 2002). However, it also suffers the tidal range problem. As the water level changes, gesture of the floating buoy will change as well, leading to an efficiency decline, as shown in Fig. 1. Until now, they have not given out a good solution. This type of WEC is now being further developed by Eco Wave Power (EWP) and several power plants have been deployed.

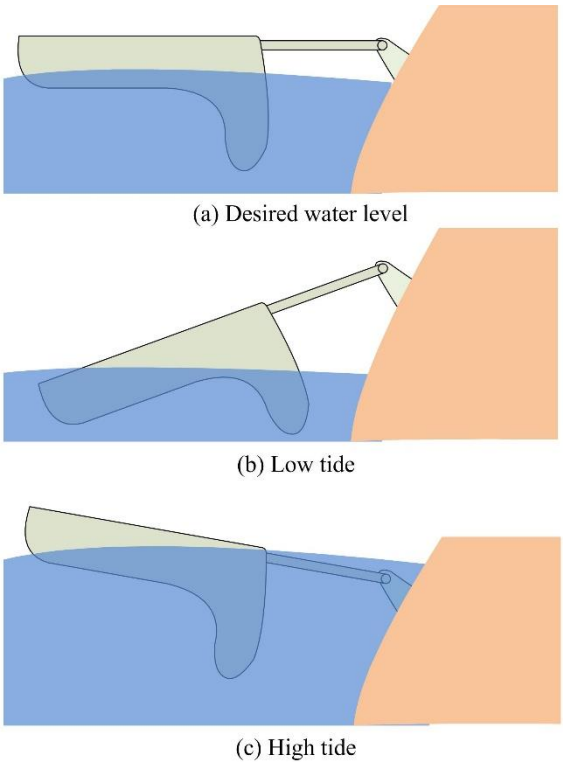

Fig. 1 Tide range's influence on classic shoreline device

There are examples of shoreline devices that taking account of water level changes. Wavestar extracts energy by directly converting the waves into an oscillating mechanical motion by using a float with a smaller extension than the average wave length (Gaspar et al., 2016; Hansen and Kramer, 2011; Zurkinden et al., 2014). In their design, the base can move up and down along a set of piers to follow the tide. Another example is the Drakoo wave energy device, developed by Hann-Ocean Energy in Singapore. This modularized shoreline device transforms waves into a continuous water flow that drives a hydro turbine generator. The contact section between Drakoo and the dock are designed as an unsmooth rubbery rail. Only the net buoyancy change could push it move up and down. Thus, it achieved the tide adaptation easily without imposing a burden on normal working condition.

This paper introduces an innovative floating pendulum WEC with the consideration of tide range. Firstly, the buoy's hydrodynamic shape is optimized in order to achieve a higher wave energy absorbing efficiency. Secondly, in order to keep this buoy always working at its optimum working condition no matter what the water level is, a unique rotating mechanism is designed, which is the so-called tide adaptation

mechanism. Furthermore, the numerical models are built, aiming to evaluate the design effects. The remainder of this paper is then organized as follows: Section 2 gives the description of the novel WEC. Section 3 introduces the optimization process of the buoy's hydrodynamic shape. Both the novel WEC and ordinary floating pendulum WEC are analyzed numerically in Section 4 in order to contrast effects taken by tide adaptation mechanism. The results of simulation and contrast are exhibited and discussed in Section 5.

2. Design concepts

As shown in Fig. 2, the novel WEC includes four main parts: a floating buoy, a base fixed on the seabed, a hydraulic cylinder and a unique rotating mechanism. The rotating mechanism consists of a connecting rod, a chain and two chain wheels that are exactly the same but fixed on different components, namely, the buoy and the base. Both ends of the connecting rod are hinged by rotating shafts so that no other component is rigid connected to it. Under the constraints of the chain, two chain wheels always rotate the same angle, which means that two chain wheels are always in the same phase. As one of them is fixed on the base, no rotating will occur, and then the other chain wheel could only translate along the circumference that is mapped out by the rotating connecting rod. Therefore, the buoy where chain wheel is fixed can always keep its well-designed leading edge facing the incoming wave without being affected by water level.

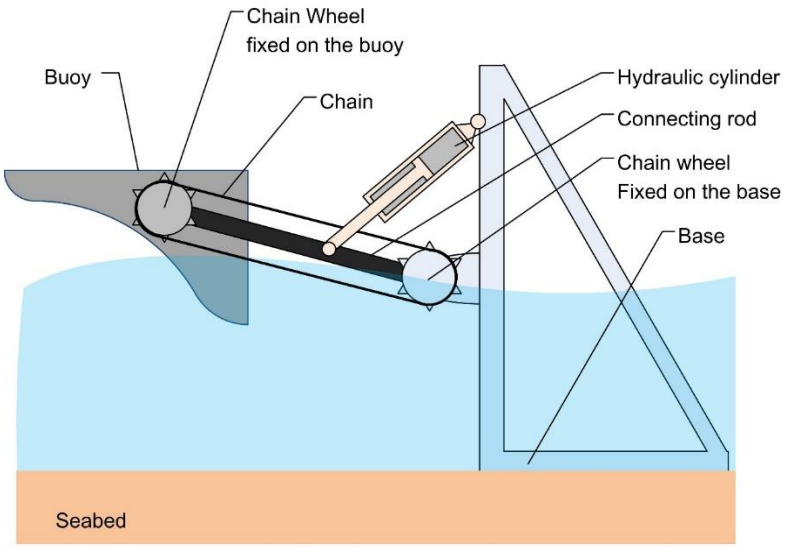

Fig. 2 Sketch of the novel WEC

The base of the novel WEC could be specially constructed, but an existing dock or jetty can also be adopted. In principle, the pivot point should be placed in the middle part of the base's tidal region. The reasons are as follows:

- According to the geometrical knowledge, if the floating pendulum oscillates approximately at the same level with the pivot point, the rotational angle could be larger in the same wave range.
- It can work normally when water level is above or beneath the pivot point. The ability to adapt the tidal range can be enhanced.
- When storm comes, the buoy can be pulled out of the water or can be pushed submerged under the water, which plays the protective function.

Hydraulic systems are pervasive in all sorts of WEC systems because of the ability to convert the oscillating motion to a relatively stable output. Waves apply large forces at slow speeds and hydraulic systems are suited to absorbing energy under this regime. Moreover, it is a simple matter to achieve short-term energy storage, necessary to achieve the smooth electricity production required for a marketable machine, with the use of cheap and available high-pressure gas accumulators (Henderson, 2006). For the novel WEC, the hydraulic system is always the best choice. However, in this paper, in order to simplify the modeling, the power-take-off (PTO) is replaced by a damping, which is believed to make no considerable difference on contrasting outputs of WECs

with or without tide adaptation mechanism.

3. Optimization of buoy's hydrodynamic shape

Hydrodynamic characteristic is one of the crucial factors that effects novel WEC's energy conversion efficiency. Even a little change, for example introducing a rounded corner, will result in completely different hydrodynamic quality (Taylor et al., 2016; Zhang et al., 2015). For the floating buoy adopted in this paper, the outline can be divided into three parts: leading edge, trailing edge and upper edge. Since the upper edge has no contact with the water, it can be designed to be flat or, taking into account aesthetics, fan-shaped. The trailing edge plays a secondary role on deciding buoy's hydrodynamic performance. The incoming wave has already been attenuated after it goes through the leading edge. Therefore, we just design the trailing edge nearly orthogonal to the connecting rod in order to reduce the energy loss by radiation during the buoy's oscillation. The leading edge has a dominant influence on buoy's hydrodynamic performance. In this paper, the exhaustion method is adopted. By using a computational fluid dynamics (CFD) software and compare each one's oscillating performance, it becomes possible to optimize the leading shape. However, it should be noticed that such an optimization strategy is not optimal but rather sub-optimal.

Firstly, five basic shapes are sketched and shown in Fig. 3. All of these five basic buoys are designed with the same rotational inertia and fluid-solid contact area at undisturbed water, which gives them the same hydrostatic stiffness. Thus, without considering the incoming wave, there is no other factor that effects the buoy's hydrodynamic performance but the shape. The following job is to establish models of these five buoys and run a time-domain simulation in CFD software-FLOW3D that is a RANSE (Reynolds Averaged Navier Stokes Equations) solver. The improved volume of fluid technique (truVOF) it adopted has great convenience for tracking and locating the free surface of fluid, meanwhile, the FAVOR^{TM} technique that based on the concept of area fraction and volume fraction of the rectangular structured mesh is very helpful

for the meshing of rigid body (Flow Science Inc., 2008). In addition, settings of the wave maker is very considerate. This software has long been widely applied to the interaction between wave and floating bodies (Bhinder et al., 2015).

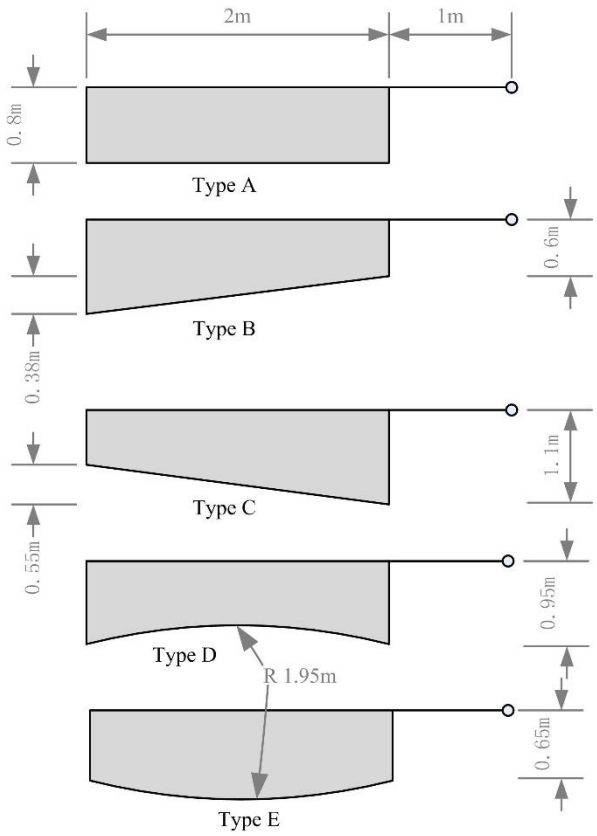

Fig. 3 Five basic shapes for comparison

As FLOW3D is a time-domain CFD solver, so selecting proper input wave parameters is an important precondition for gaining helpful simulation results. It is important to specify here that the optimization of buoy's shape is not for academic purpose only, in the future, the designed novel WEC is desired to be built and run on Zhoushan, China. Thus, a typical wave condition ($T_1 = 5s, H_1 = 1m$) in Zhoushan is chose as a set of input wave parameters (Wang et al., 2011; Zhang et al., 2009). In consideration of wave's effects on buoy's hydrodynamic performance, other two wave conditions ($T_2 = 3s, H_1 = 1m;\ \ T_3 = 7s, H_3 = 1m$) are also added into the simulation. It should be pointed out that the wave tank depth is set as 10 m in order to match the shoreline water depth, and no PTO mechanism is introduced in these simulations. The main solver properties for the three dimensional simulations conducted in FLOW3D is shown in Table 1. In addition, the user defined input parameters are presented in Table

2. The buoy's mass is set distributed evenly. One constraint is added to ensure that only rotation around pivot point will occur.

Table 1 Properties for FLOW3D calculation

Flow model	Incompressible
Number of fluid	One fluid
Moving Object Model	Implicit
Turbulent Model	Renormalized group (RNG) model
Pressure Solver	Implicit, GMRES
Volume of Fluid Advection	Split Lagrangian Method
Momentum Advection	Second order monotonicity preserving

Table 2 Input parameters for FLOW-3D simulation

Waveform function	Linear wave
Wave period	Case1=3s; Case2=5s; Case3=7s
Wave height	1m
Depth of water	10m
Density of buoy	300kg/m^3

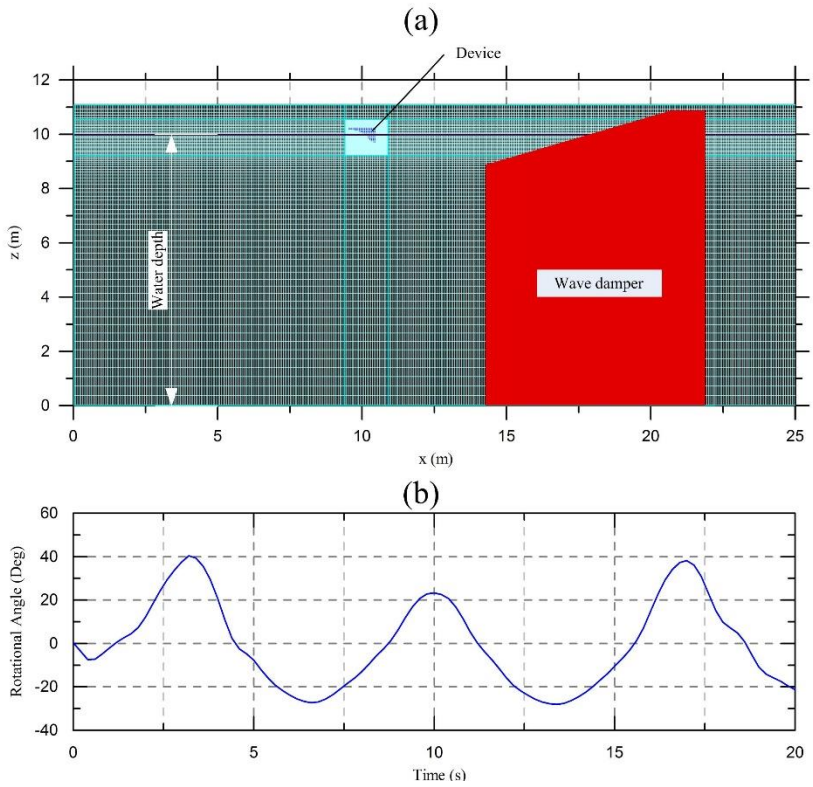

Fig. 4 Meshing and output of a set of calculation

Before the simulation, getting a good mesh profile has an important effect on increasing the calculation accuracy. On the other side, excessive small girds will spend much more calculation time. For the mesh in this example, grids in focus area are subdivided (see Fig. 4(a)), which increase the calculation accuracy without affecting the efficiency too much. Useful results, like rotational angle (as shown in Fig. 4(b)), are obtained after simulations. As the rotational angle is proportional to the maximum potential energy that the floating buoy can harness under wave's driving, it is finally selected to evaluated buoys' hydrodynamic performance. The comparison results of all five kinds of buoy in three wave conditions are presented in Fig. 5. The figure of type C seems have the biggest rotational angle under three typical wave conditions, which means that the leading edge should be designed outward-inclined.

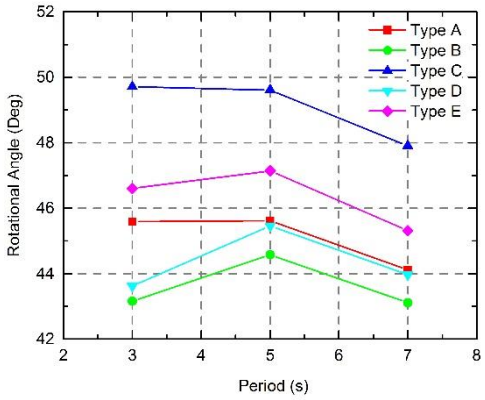

Fig. 5 Comparison of five buoys' rotational angles

However, whether the slope should be designed flat or uneven is still unknown. Thus, further optimizations are still needed to further refine the slanted plane. In this step, the slope is divided into two parts (theoretically, dividing into more parts will give out better optimization quality. However, on the other hand, it will sacrifice more simulation time. Dividing into two parts is a trade off between simulation efficiency and optimization quality). Different points are chosen as the turning point of the curved surface: the midpoint or the lower quarter point (as shown in Fig.6). Curve on one side is designed to be tangential to the curve on the other side. Under these preconditions, two styles are available: convex first and then cuppy (S-shaped) or cuppy first and then convex (Reverse S-shaped). Our analysis indicates that the sharp corner in the bottom of the S-shape buoy will lead to significant vortex shedding, which will effect energy conversion efficiency dramatically. Thus, we finally choose the reverse S-shape as the basis of our further optimization. Depend on different turning points and tangency angles, six types of buoys are exhibited in Fig.6. Three types in the first column take the midpoint as turning point of two curves, while other three take the lower quarter point as the turning point. Each row in this figure has the same tangency angle, varying from 45 degree to 75 degree.

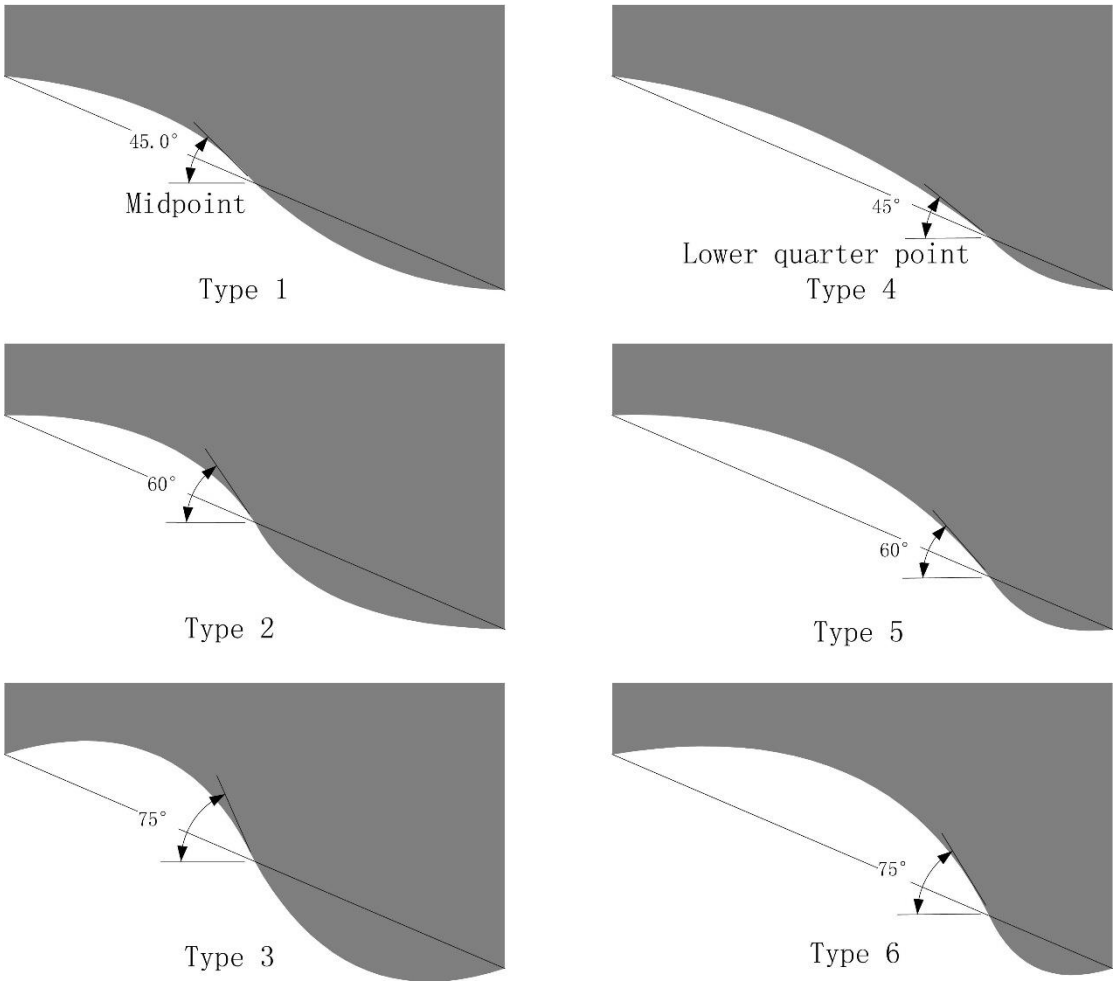

Fig. 6 Six further designed buoys

Three sets of wave parameters ($T_1 = 3s, H_1 = 0.8m;\ T_2 = 5s, H_2 = 0.8m;\ T_3 = 7s, H_3 = 0.8m$) are adopted in the simulations in this link. The comparison results are shown in Fig. 7. It can be seen that when incoming wave period is small, type 5 has the largest rotational angle, while type 3 has the largest rotational angle as wave period increases. In conclusion, if the wave period in the testing site is smaller than 4.3s, buoy with type 3 has the better performance, while if the wave period is larger than 4.3s, type 5 has the better performance. Until now, the design of leading edge has been finished, and as a result, two best curves (type 5 for high frequency waves, while type 3 for small frequency waves) are recommended after comparisons. As the testing site of our wave tank could only make wave with periods smaller than 5s, type 3 is finally chosen as the basis of our design. The vertical face in front of the buoy is covered with an arc to streamline the leading edge. Our ultimate shape that fits small periodic wave is exhibited in Fig. 8, in which the part painted light green is type 5 in

Fig.6 and the light blue part is the new introduced arc.

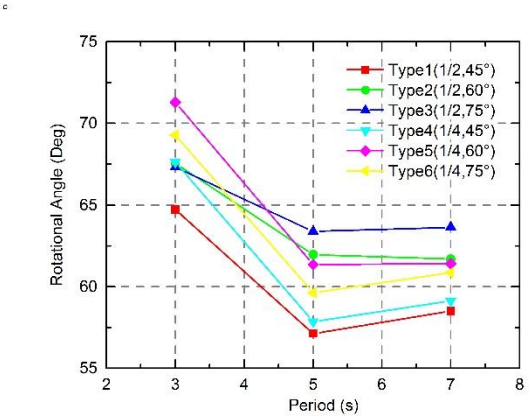

Fig. 7 Comparison of six buoys' rotational angles

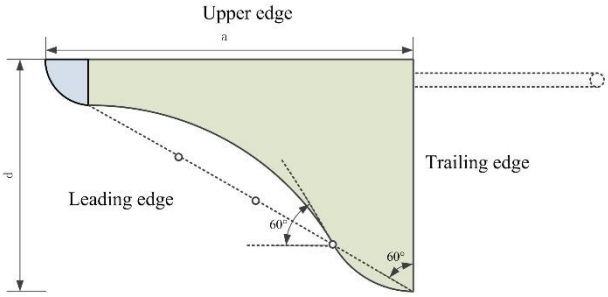

Fig. 8 The optimized buoy shape

4. Modelling

As the novel floating pendulum WEC has a special rotating mechanism (as introduced in Section 2), its mathematical analysis is greatly different from classic floating WEC. In this section, the novel WEC will be analyzed in detail. In order to achieve a more precisely simulation, several crucial parameters are going to be further discussed before establishing the MATLAB/Simulink model. In the last subsection, ordinary floating pendulum WEC will be analyzed to help building the reference model.

4.1 Coordinate system

The global coordinate of the model are $\begin{pmatrix} x_A \\ z_A \end{pmatrix}$ and the local coordinate $\begin{pmatrix} x_B \\ z_B \end{pmatrix}$ are the coordinate for the oscillating buoy. For each WEC, there exists:

$$^{A}\boldsymbol{P} = {}^{A}_{B}\boldsymbol{R}({}^{B}\boldsymbol{P} + {}^{A}_{B}\boldsymbol{T}) \quad (1)$$

Where: $^{A}\boldsymbol{P}$ and $^{B}\boldsymbol{P}$ represents the vector in different coordinate systems (the upper-left corner mark represents the coordinate system); ${}^{A}_{B}\boldsymbol{R}$ and ${}^{A}_{B}\boldsymbol{T}$ are the rotation and translation transformation matrix respectively. For the novel WEC, there is only translational motion occur (as shown in Fig. 9). Therefore, the transformation matrixes can be expressed as:

$${}^{A}_{B}\boldsymbol{T} = \begin{pmatrix} -l\sin\theta \\ l\cos\theta \end{pmatrix} \quad (2)$$

$${}^{A}_{B}\boldsymbol{R} = \begin{pmatrix} 1 & 0 \\ 0 & 1 \end{pmatrix} \quad (3)$$

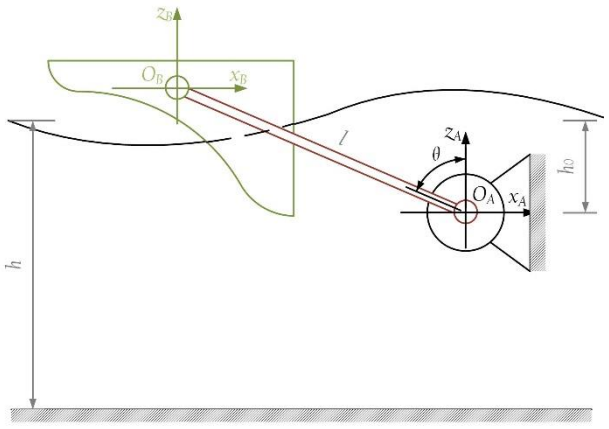

Fig. 9 Coordinate systems of the novel WEC

4.2 Dynamic analysis

Analysis in this section aims to build a time domain simulation model of novel WEC. Considering the displacement and velocity of the buoy under irregular waves may lead to results that is close to the actual working condition. However, it also made the model much more complicated. In this paper, a simulation model under regular wave is enough to certify the WEC's tide adaptability. For a regular wave, the water level function can be illustrated as:

$$^{A}\boldsymbol{A}(x,t) = \left(\frac{H}{2}\sin\left(\omega t - 2\pi\frac{x}{\lambda} + \varphi\right)\right) \quad (4)$$

Where: H is the wave height; ω is the wave frequency; λ is the wave length, and

there exists: $\lambda = 2\pi/k$, in which k is the wave number and it satisfies $\omega^2/gk = \tanh kh$; φ is the initial phase difference.

The wave power can be described as:

$$P_{wave} = \frac{\rho g^2 T H^2}{64\pi} \tag{5}$$

Where: T is wave period, ρ is water density and g is gravity acceleration.

In order to evaluate WEC's performance, the term efficiency has began to be displaced by capture width, which is a parameter defined as the width of the wave front that contains the same amount of power as that absorbed by the WEC (Price et al., 2009).

$$Cw = \frac{P_{WEC}}{P_{wave}} \tag{6}$$

Where P_{WEC} is the absorbed power by WEC.

The main distinctive feature in the novel WEC that can keep the leading edge of the buoy facing the incoming wave all the time is its special rotating mechanism. There is only translation occurs in the floating buoy's oscillating process. Based on dynamics of rigid body when transport motion is translational, sum of moments on O_B has to be zero to ensure no rotation will occur. Therefore, we have the first equation of motion:

$$^{B}M_{eB} + {}^{B}M_{rB} + {}^{B}M_{bB} + {}^{B}M_{dB} + {}^{B}M_{aB} + {}^{B}M_{chain} = 0 \tag{7}$$

Where: $^{A}M_e$ is excitation moment applied by the incoming wave; $^{A}M_r$ is radiated moment acting on the wetted face of the buoy; $^{A}M_b$ is hydrostatic moment; $^{A}M_d$ is the drag moment; $^{A}M_{PTO}$ is the reacting moment of PTO; $^{B}M_{chain}$ is moment applied by the chain. The added *B* in the subscript means that they are moments relative to O_B.

Then, the floating buoy can be considered as a mass point on the global coordinate system. Based on Newton's second law, we have the second equation of motion:

$$J_A\ddot{\theta} = {}^{A}M_{eA} + {}^{A}M_{rA} + {}^{A}M_{bA} + {}^{A}M_{dA} + {}^{A}M_{chain} + {}^{A}M_{PTO} \tag{8}$$

Where: J_A is the rotational inertia about pivot point O_A, there exists $J_A = ml^2$ in which m is mass of the buoy; $^{A}M_{chain}$ is moment applied by the chain acting on O_A. Other characters have the same meaning as in Equation 7. The added *A* in the subscript means that they are moments applied on O_A.

The PTO system here is modeled as a linear damper. Hence, it can be demonstrated

as:

$$^{A}M_{PTO} = c_{pto}\dot{\theta} \tag{9}$$

Then, the absorbed power by WEC P_{WEC} can be obtained easily:

$$P_{WEC} = {}^{A}M_{PTO}\dot{\theta} = c_{pto}\dot{\theta}^2 \tag{10}$$

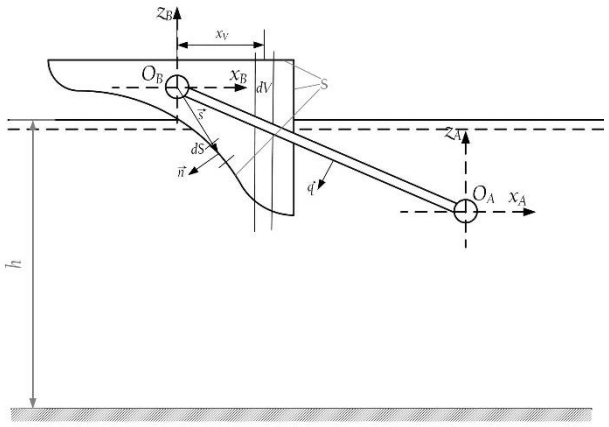

Fig. 10 Diagram of integration method for novel WEC analysis

4.3 Non-linear hydrostatic moment

It is widely acknowledged that upward buoyant force that is exerted on a body immersed in the fluid, whether fully or partially submerged, is equal to the weight of the fluid that the body displaces and it acts in the upward direction at the center of mass of the displaced fluid based on Archimedes' principle. For irregularly shaped buoy, like the one shown in Fig.8, nonlinearity of geometry and the ever-changing moment arm will lead to a highly nonlinear input-output relation. The hydrostatic moment is obtained by integral over the wetted surface S:

$$^{B}M_{bB} = \iint_S p_b|\boldsymbol{n} \times \boldsymbol{s}|dS \tag{11}$$

$$^{A}M_{bA} = \iint_S p_b l\boldsymbol{n} \cdot \boldsymbol{q}dS \tag{12}$$

Where: p_b is the hydrostatic pressure acting on element dS; Vector $\boldsymbol{q}$ gives the position of dS, where its unit normal vector is $\boldsymbol{n}$.

The hydrostatic pressure p_b can be expressed as:

$$p_b = \rho g z \tag{13}$$

Where z is the depth of the surrounding water.

Based on Equation 11 to equation 13, we obtained the relationship between the rotational angle and the hydrostatic moments, just as shown in Fig. 11. The point A in the upper curve indicates that when the buoy is completely submerged and the connecting rod is horizontal, the hydrostatic moment ${}^{A}M_{bA}$ reaches a maximum value. After that, although the buoyancy force acting on the buoy hold steady, ${}^{A}M_{bA}$ begins to decrease as the force arm changes. After abscissa of the buoyant center become positive (point B in Fig. 11), ${}^{A}M_{bA}$ sees an increase on the positive direction.

As the buoyant center and the buoy's pivot do not coincide in this buoy, the hydrostatic moment ${}^{B}M_{bB}$ tends to increase with rotating angle (as shown in the lower curve in Fig. 11). At point C, part on the left side of O_B begins to submerge into the water. And at point D, all parts have been completely submerged.

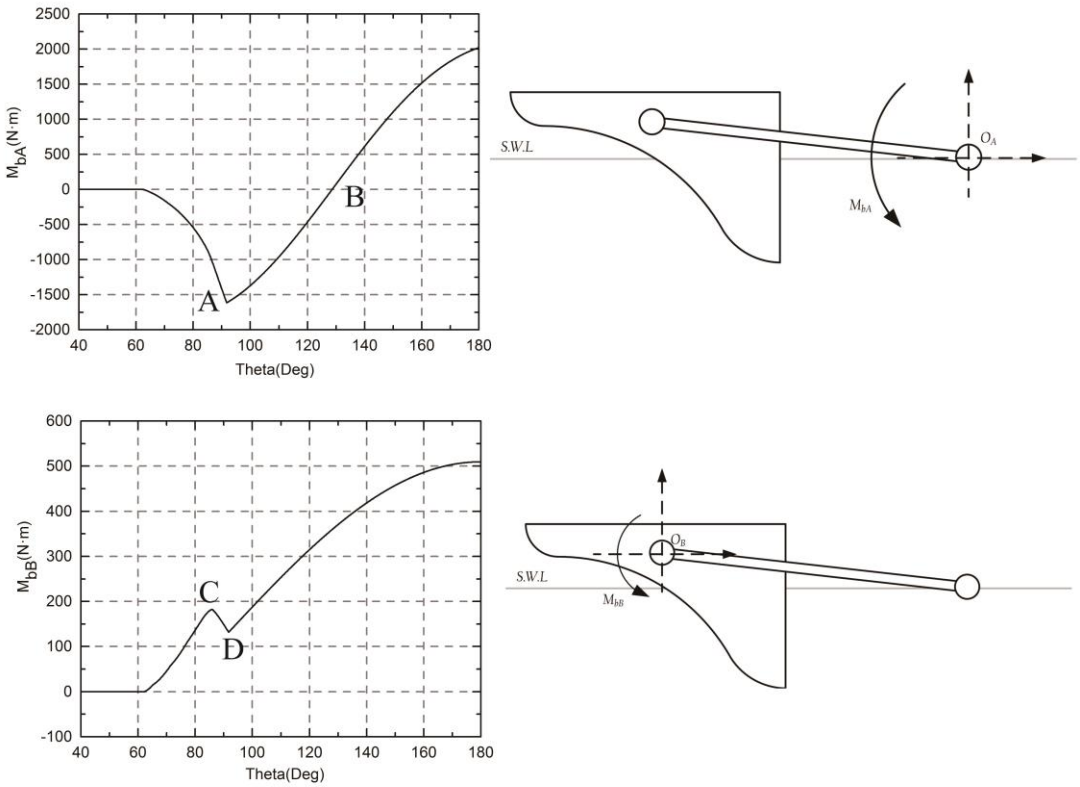

Fig. 11 Relationship between rotational angle and hydrostatic moment

Judging from the results of the analysis, simplify the hydrostatic moment as proportional to the rotational angle, like the frequency domain simulation models have done, will lead to great calculation error (Gomes et al., 2015). However, a time domain one is able to analyze non-linear force or moments accurately.

4.4 Wave and float interaction

The hydrodynamic moment acting on the buoy can be computed from velocity potential ϕ based on the potential flow theory. If the body is fixed, no radiated wave is generated, and then we have the excitation moment M_e in such a case. Excitation moments M_e on the element dS in terms of different rotation centers are given respectively as:

$$^{B}M_{eB} = \iint_S p_e(\boldsymbol{n} \times \boldsymbol{s})dS \tag{14}$$

$$^{A}M_{eA} = \iint_S p_e l\boldsymbol{n} \cdot \boldsymbol{q}dS \tag{15}$$

Where p_e is the excitation pressure that applied on element dS.

The excitation pressure p_e is calculated as:

$$p_e = -i\omega\rho\phi_e \tag{16}$$

Where ϕ_e is velocity potential of the incident wave (Falnes, 2002).

$$\phi_e = -\frac{g}{i\omega}\frac{e^{k(z+h)}+e^{-k(z+h)}}{e^{kh}+e^{-kh}}A \tag{17}$$

Where: k is the wave number; A is the real-time wave height; z is the depth of the surrounding water and h is the depth of wave tank.

Another case is when the body is oscillating in the absence of an incident wave, the forces and moments acting on the body which are due to the radiated wave caused by the body's oscillation are called the radiation force (moment). It is also labelled with a subscript of lowercase *r*. Based on the linear potential theory the radiation force (moment) is represented as a function of added mass and radiation damping both are 6 $\times$6 matrices for a general three dimensional analysis. In order to reduce the difficulty in simulation, just like the analysis of similar structures-Wavestar and M4 wave energy devices do, a simpler approach is adopted: the buoy responds in a vertical plane (Hansen and Kramer, 2011; Taylor et al., 2016). In regular waves, the radiation force in vertical direction can be expressed as:

$$F_r(\omega) = a_{33}(\omega)\ddot{x} + b_{33}(\omega)\dot{x} \tag{18}$$

Where the parameter a_{33} is referred as the added mass and b_{33} is the radiation damping coefficient of heave. They are related to reactive energy transport in the near-

field region of the oscillating buoy. For the special buoy geometry here, these two parameters can be obtained by WAMIT, a package that is based on BEM (boundary element method) and have been widely used for WEC's analysis (Babarit et al., 2012; Li and Yu, 2012). For the special buoy shown in Fig. 8 the parameters obtained by WAMIT is shown in Fig. 12.

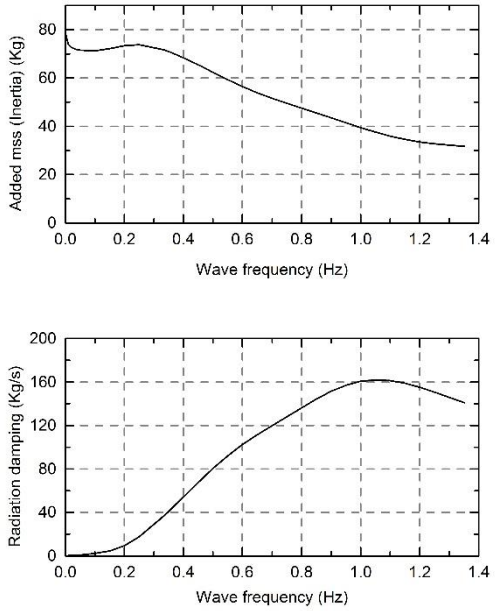

Fig. 12 Radiatin parameters given by WAMIT

The optimal strategy to get a precise value of radiation moment is to integral over the wetted surface based on the hydrodynamic pressure acted on the buoy. However, this method is so inconvenient that may bring a lot of troubles only with slight calculation accuracy improvement. A compromised method is to figure out an equivalent force arm that can obtain the radiation moment by multiplying the radiation force in Equation15. As the submerged geometry of the float here is not axisymmetric about a vertical axis, the equivalent point of application of radiation moment on the buoy is chosen as the center of gravity of the immersed part of the buoy. Then, radiation moments based on two turning points O_B and O_A can be expressed as:

$$^{B}M_{rB}(\omega) = F_r(\omega) l_{GB} \tag{19}$$

$$^{A}M_{rA}(\omega) = F_r(\omega) l_{GA} \sin\theta \tag{20}$$

Where l_{GA} is the distance between the center of gravity of the immersed part of the buoy and O_A, while l_{GB} is the distance between the center of gravity of the

immersed part of the buoy and O_B.

4.5 Representation of drag coefficient

Generally, the viscous damping effect that follows the drag term in Morison's equation (Morison et al., 1950) can be expressed as:

$$f_d = \frac{1}{2}\rho C_D A_c (u - u_b)|u - u_b| \tag{21}$$

Where C_D is the drag coefficient, whose value depends on the body geometry, the Reynolds number and the Keulegan-Carpenter number (Li and Yu, 2012); A_c is the characteristic area; u is the velocity of the water particle while u_b is the velocity of the buoy. Both these two velocities can be decomposed into horizontal and vertical components:

$$u_x = \frac{gkA}{\omega}\frac{\cosh k(z+h)}{\cosh kh}\sin\left(\omega t - \frac{2\pi x}{\lambda}\right) \tag{22}$$

$$u_z = \frac{gkA}{\omega}\frac{\sinh k(z+h)}{\cosh kh}\cos\left(\omega t - \frac{2\pi x}{\lambda}\right) \tag{23}$$

Where: x is the horizontal ordinate of the water particle and $\lambda = (T^2 g)/2\pi$ is the wave length.

The horizontal and vertical components can be easily calculated based on the buoy's angular velocity and its shape function. Overall drag moment can be obtained by an integral over the wetted surface:

$$M_d = M_{dx} + M_{dy} = \int_S f_{dx} l' \cos\theta \, dS + \int_S f_{dy} l' \sin\theta \, dS \tag{24}$$

Where: l' is the distance between the element dS and the pivot point.

The rotational angle of novel WEC with various drag coefficients are plotted in Fig. 13. It is consistent well with a recent research carried out by *Babarit(2012)*. They changed the drag coefficients from one quarter to twice their nominal values, and finally found that the uncertainty associated with drag effects can be negligible when the heaving buoy is fixed on a platform. In this paper, we adopted a drag coefficient suggested by Flow-3D. However, an effective drag coefficient dependent on wave height and possibly period is needed to calibrate by conducting additional wave tank tests(Stansby et al., 2015; Yeung et al., 1998).

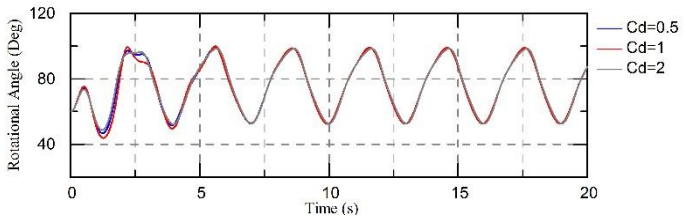

Fig. 13 Simulation results of the novel WEC under various drag coefficients. The WEC is drived by regular wave: wave height= 0.3m, wave period=3s.

4.6 Modelling of ordinary floating pendulum WEC

Due to the ordinary motion mechanism, all elements of the ordinary floating WEC rotates around the turning point O_A, which makes it much more easier to build the numerical model of ordinary floating WEC. Although, the coordinate system in classic floating WEC (just as shown in Fig. 14) is much different from the novel WEC, the coordinate transformation formula Equation1 also works here. However, matrixes ${}^{A}_{B}\boldsymbol{R}$ and ${}^{A}_{B}\boldsymbol{T}$ should take diverse values:

$$ {}^{A}_{B}\boldsymbol{T} = \begin{pmatrix} -l \\ 0 \end{pmatrix} \tag{25} $$

$$ {}^{A}_{B}\boldsymbol{R} = \begin{pmatrix} \sin\theta & -\cos\theta \\ \cos\theta & \sin\theta \end{pmatrix} \tag{26} $$

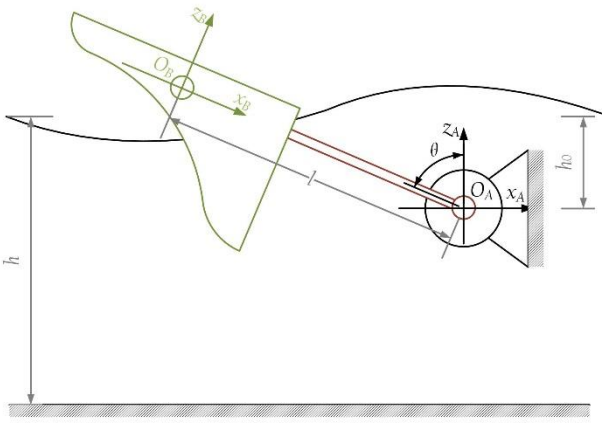

Fig. 14 Coordinate systems of classic floating WEC

As there is only one degree of freedom, the analysis becomes much easier. The buoy motion can be obtained following the Newton's second law:

$$ J_m\ddot{\theta} = {}^{A}M_e + {}^{A}M_r + {}^{A}M_d + {}^{A}M_b + {}^{A}M_G + {}^{A}M_{PTO} \tag{27} $$

Where: ${}^{A}M_e$ is excitation moment applied by the incoming wave; ${}^{A}M_r$ is radiated moment acting on the wetted face of the buoy; ${}^{A}M_d$ is the drag moment; ${}^{A}M_b$ is the hydrostatic moment; ${}^{A}M_G$ is the gravity moment; ${}^{A}M_{PTO}$ is the reacting moment of PTO.

The analysis of wave and float interaction in section 4.4 can also be used to build the ordinary floating pendulum's numerical model.

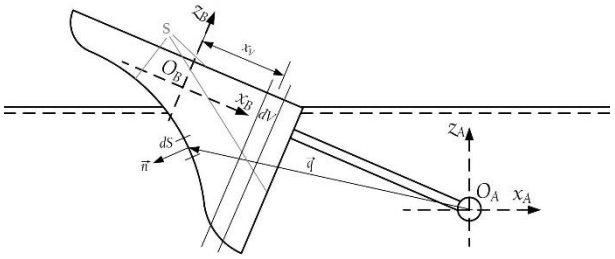

Fig. 15 Diagram of integration method for classic floating WEC analysis

Like the novel WEC, the hydrostatic moment of classic floating WEC should be calculated a face integral over the wetted surface S(as shown in Fig. 15):

$$ {}^{A}M_b = \iint_S p_b l(\boldsymbol{n} \cdot \boldsymbol{q}) dS \tag{28}$$

Where: p_b is the hydrostatic pressure acting on element dS; Vector $\boldsymbol{q}$ gives the position of dS, where its unit normal vector is $\boldsymbol{n}$. In addition, Equation10 still works here. Therefore, the hydrostatic moment ${}^{A}M_b$ can be figured out, just as shown in Fig. 16. Before the buoy is completely submerged, the absolute value of hydrostatic moment increases non-linearly because of the buoy's special profile. Then it begins to decrease as the force arm changes. Until abscissa of the buoyant center become positive, ${}^{A}M_b$ begins to increase on the positive direction. What has to be explained is that Fig. 16 only presents the hydrostatic moment change when the deployment depth h_0 is 0, 0.2 and -0.2. If the deployment depth is changed to other values, the absolute values and turning points may change as well. However, the variation trends will not change significantly.

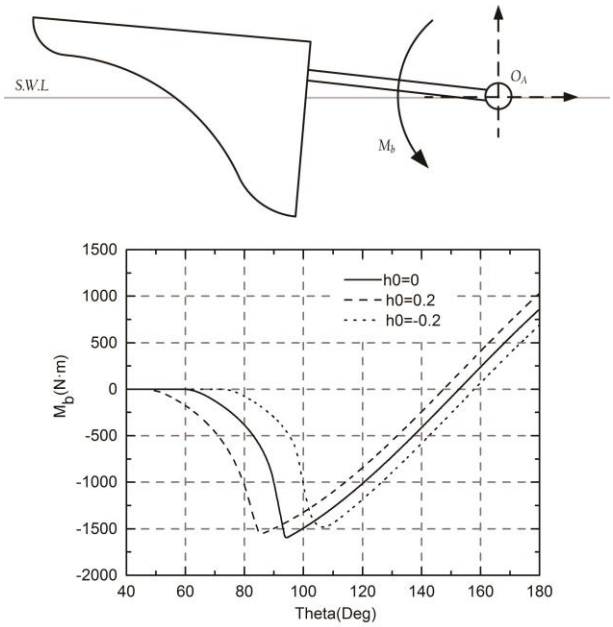

Fig. 16 Relationship between rotational angle and hydrostatic moment in classic floating WEC

5. Time-domain simulations

Dynamic simulation models of both two WECs have been built in MATLAB/Simulink in order to compare these two WECs, which can also guide the later wave tank experiment. Key parameters in simulations are exhibited in Table 3. The length a and height d of the buoy is as shown in Fig.8, while the width b is the thickness of the buoy in Fig.8. These simulations aim to investigate how the output would change with the water levels. Therefore, various sets of displacement depth are adopted to represent the water level change, while water depth is set as a constant in order to ensure the wave force will hold steady in different water levels.

Table 3 Setting parameters for simulations

Wave height (H)	0.5m
Wave period (T)	Case1: 4s
	Case2: 5s
	Case3: 6s
Depth of water (h)	10m

Depth of displacement ($h0$)		-0.5m~0.2m
Straight-line distance between O_A and O_B (l)		1m
Parameters of buoy	Length (a)	0.8m
	Width (b)	1m
	Height (d)	0.5m
	Density (ρ_{buoy})	300kg/m^3

A basic control strategy called classic linear passive control strategy is adopted in the numerical models. The damping coefficient of PTO is constant during operation process. For a damping PTO, the power of output can be computed based on Equation10. Therefore, for each displacement depth, various PTO reacting moment may lead to different output power and efficiency. The PTO mechanism should be optimized firstly to guarantee a satisfied damping coefficient c_{PTO} (show in Equation10) is adopted when there is no advanced control strategy involved.

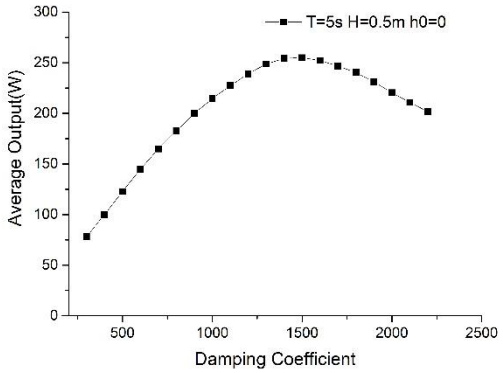

Fig. 17 Influence of damping coefficient on average output of novel WEC

As shown in Fig. 17, the figure of average output of novel WEC increase steadily in the beginning, and the highest value appears when damping coefficient $c_{PTO} = 1500$, after which it begin to decrease. That means when the damping coefficient is not large enough, the kinetic energy can't be absorbed completely, but once it is set too large, the rotational angle will be effected dramatically, which will lead to a relatively lower power output. The damping coefficient corresponding to the pole can be considered as the optimal damping coefficient (ODC) in the certain deployment depth.

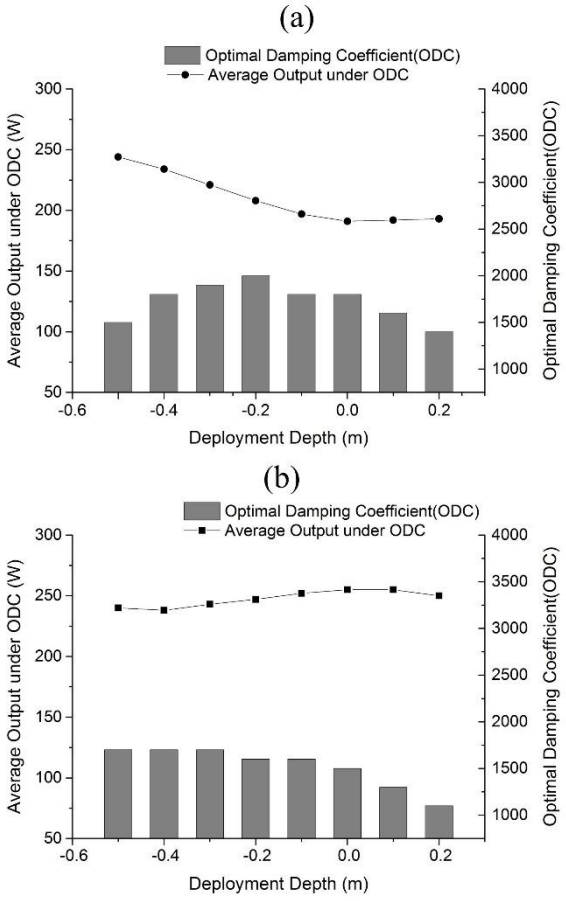

Fig. 18 Influence of deployment depth on average output. (a) ordinary, T=5s, H=0.5m; (b) novel, T=5s, H=0.5m

In Fig. 18(a) various deployment depth are adopted. The bar chart shows the ODC for each deployment depth while the line chart compares the average output under ODC under a wave condition with T=5s, H=0.5m. The deployment depth is the distance between O_A and still water level. When it is positive, it means O_A is under water, and vice versa. The figure shows that the average output of ordinary floating pendulum WEC varies from 191W to 244W, fluctuating by as much as 27.7%. The output reaches its peak when the deployment depth is -0.5m and the damping coefficient is 1500. Correspondingly, simulation results of the novel WEC are exhibited in Fig. 18(b). In the deployment depth range from -0.5~0.2m, the average output under ODC varies from 238W to 255W, fluctuating by only 7.1%. The figure reaches peak output when the deployment depth is 0.1m and the damping coefficient is 1300.

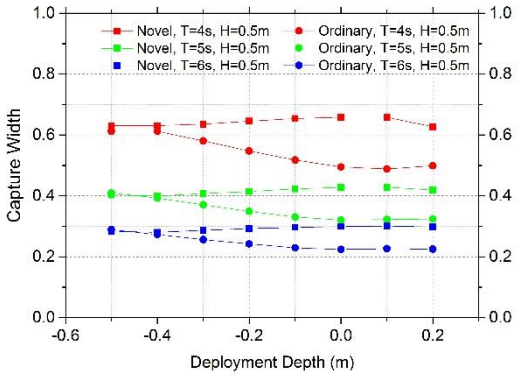

Fig. 19 Comparison of average output

Comparison results of these two WECs in terms of different wave conditions are presented in Fig. 19. It is clear that by adopting tide adaptation mechanism, the ability to adapt varying water levels has been enhanced greatly. It seem that the difference making by tide adaptation mechanism will be greater as if the wave frequency is getting closer to the buoy's natural frequency which is estimated to be 0.625Hz. It is interesting that when compared with the ordinary floating WEC, the novel WEC always has a higher efficiency in all deployment depth. One possible reason for this relates to that the buoy's gesture is holding horizontal all the time even in the wave range. The chain drive system might be another cause. When the pivot in the buoy is located in the front part, M_{chian} figured out from Equation7 will have positive contribution to the buoy's rotational acceleration. However, it is just an inference now, evidences we got from simulation results are still not enough to prove this hypothesis. If it is confirmed by additional model or experiments this would clearly be beneficial.

Some of our wave conditions are not linear enough due to their large wave height and wave length ratio. Adopting linear wave theory will lead to larger calculation errors. Zurkinden et al. (2014) have compared the simulation results of linear numerical model and non-linear numerical model with experimental results under the similar wave conditions. The results indicate that the advantage of non-linear wave theory (Stokes, higher order) over linear wave theory in calculation accuracy is not significant. Thus, it is reasonable to consider that the calculation errors taking by adopting linear wave theory is acceptable here.

6. Conclusions

In this paper, we have introduced our novel floating pendulum WEC, comprising the base and buoy connected by chain drive system. The aim is to keep the well-designed incoming edge facing the income wave straightly in various water levels, which is believed to be helpful for improving energy conversion efficiency, regardless of tide range. In order to guarantee the tide adaptation mechanism works meaningfully, the buoy's hydrodynamic shape should be optimized firstly. This has been achieved through a CFD software-Flow3D, by enumerating several kinds of typical profile and comparing their hydrodynamic performance. After a two-stage optimization, suggested results are shown in terms of wave conditions.

In order to compared the novel WEC to traditional floating pendulum WEC, numerical models of both devices are built respectively. There are approximations inherent in the analysis, and uncertainties regarding the effects of viscosity on the responses of the buoy. The torque induced by vortex-shedding at body edges is also ignored in this paper. However, when the PTO is taken into consideration, the impacts induced by these uncertainties are found to be negligible.

A basic control strategy, called classic linear passive control is adopted to design the PTO. An optimal damping coefficient is set as an invariant during the operation process. After several sets of simulation, we finally clarify the relationship between the wave devices' outputs and the water levels. The comparisons of the results of modelling for two devices in regular seas lead to the following findings:

1) The scaled wave device designed with tide adaptation mechanism has a steady output, with a fluctuation of only 10%, when the displacement depth range from -0.5m to 0.2m. It means that it has the ability to adapt a tide range of 0.7m. On the contrary, the output of wave device without tide adaptation ability changes with water levels in a wide range.
2) The wave device designed with tide adaptation mechanism has a larger output than the one without tide adaptation mechanism in tide range of -0.5m~0.2m. It indicates

that either the chain link system or the straightforward leading edge contributes positively to the device's energy conversion efficiency.

The study to date has suggested two kinds of buoy shapes for floating pendulum WEC, and has verified the feasibility of tide adaptation mechanism in regular waves. A wave device of third to fourth the model's size is able to work functionally near most coastlines in China. Further investigation would be required to compare the output in irregular waves and find an advanced control strategy to further improve floating pendulum WEC's energy conversion efficiency.

Acknowledgements

The work was financially supported by the National Natural Science Foundation of China (No. 51579222， No. 51120195001 and No.51521064), Zhejiang Provincial Natural Science Foundation of China (No. LY15E090001) and Youth Funds of the State Key Laboratory of Fluid Power and Mechatronic Systems (Zhejiang University) No. KLoFP_QN_1604).

References:

Arman, H., Yuksel, I., 2013. New developments in renewable energy. InTech.

Babarit, A., Hals, J., Muliawan, M., Kurniawan, A., Moan, T., Krokstad, J., 2012. Numerical benchmarking study of a selection of wave energy converters. Renewable Energy 41, 44-63.

Bhinder, M.A., Babarit, A., Gentaz, L., Ferrant, P., 2015. Potential time domain model with viscous correction and CFD analysis of a generic surging floating wave energy converter. International Journal of Marine Energy 10, 70-96.

Boake, C.B., Whittaker, T.J., Folley, M., Ellen, H., 2002. Overview and initial operational experience of the LIMPET wave energy plant, The Twelfth International Offshore and Polar Engineering Conference. International Society of Offshore and Polar Engineers.

Clément, A., McCullen, P., Falcão, A., Fiorentino, A., Gardner, F., Hammarlund, K., Lemonis, G., Lewis, T., Nielsen, K., Petroncini, S., 2002. Wave energy in Europe: current status and perspectives. Renewable and Sustainable Energy Reviews 6 (5), 405-431.

Drew, B., Plummer, A., Sahinkaya, M.N., 2009. A review of wave energy converter technology. Proceedings of the Institution of Mechanical Engineers, Part A: Journal of Power and Energy 223 (8),

887-902.

Falnes, J., 2002. Ocean waves and oscillating systems. Cambridge University Press, Cambridge, UK.

Flow Science Inc., 2008. FLOW3D User Manual.

Gaspar, J.F., Calvário, M., Kamarlouei, M., Soares, C.G., 2016. Power take-off concept for wave energy converters based on oil-hydraulic transformer units. Renewable Energy 86, 1232-1246.

Gomes, R., Lopes, M., Henriques, J., Gato, L., Falcão, A., 2015. The dynamics and power extraction of bottom-hinged plate wave energy converters in regular and irregular waves. Ocean Engineering 96, 86-99.

Hansen, R.H., Kramer, M.M., 2011. Modelling and control of the wavestar prototype. Proc. EWTEC.

Henderson, R., 2006. Design, simulation, and testing of a novel hydraulic power take-off system for the Pelamis wave energy converter. Renewable Energy 31 (2), 271-283.

Li, Y., Yu, Y.-H., 2012. A synthesis of numerical methods for modeling wave energy converter-point absorbers. Renewable and Sustainable Energy Reviews 16 (6), 4352-4364.

Morison, J., Johnson, J., Schaaf, S., 1950. The force exerted by surface waves on piles. Journal of Petroleum Technology 2 (05), 149-154.

Price, A., Dent, C., Wallace, A., 2009. On the capture width of wave energy converters. Applied Ocean Research 31 (4), 251-259.

Stansby, P., Moreno, E.C., Stallard, T., 2015. Capture width of the three-float multi-mode multi-resonance broadband wave energy line absorber M4 from laboratory studies with irregular waves of different spectral shape and directional spread. Journal of Ocean Engineering and Marine Energy 1 (3), 287-298.

Taylor, R.E., Taylor, P., Stansby, P., 2016. A coupled hydrodynamic–structural model of the M4 wave energy converter. Journal of Fluids and Structures 63, 77-96.

Valério, D., Mendes, M.J., Beirão, P., da Costa, J.S., 2008. Identification and control of the AWS using neural network models. Applied Ocean Research 30 (3), 178-188.

Wang, S., Yuan, P., Li, D., Jiao, Y., 2011. An overview of ocean renewable energy in China. Renewable and Sustainable Energy Reviews 15 (1), 91-111.

World Energy Council, 1993. Renewable energy resources: opportunities and constraints 1990–2020, London.

Yeung, R., Liao, S.-W., Roddier, D., 1998. On roll hydrodynamics of rectangular cylinders, The Eighth International Offshore and Polar Engineering Conference. International Society of Offshore and Polar Engineers.

Zhang, D., George, A., Wang, Y., Gu, X., Li, W., Chen, Y., 2015. Wave tank experiments on the power capture of a multi-axis wave energy converter. Journal of Marine Science and Technology, 1-10.

Zhang, D., Li, W., Lin, Y., 2009. Wave energy in China: Current status and perspectives. Renewable Energy 34 (10), 2089-2092.

Zurkinden, A.S., Ferri, F., Beatty, S., Kofoed, J.P., Kramer, M., 2014. Non-linear numerical modeling and experimental testing of a point absorber wave energy converter. Ocean Engineering 78, 11-21.